Report on a problem studied at the UK Mathematics-in-Medicine Study Group Strathclyde 2004
< http://www.maths-in-medicine.org/uk/2004/retinal-detachment/ >

Post Re-attachment Retinal Re-detachment

Problem proposed by Alistair Fitt

Fourth Medical Study Group, University of Strathclyde, Glasgow, 14th-17th September, 2004

The contributors to the work on this problem at the Study Group were Rosemary Dyson[1], Alistair Fitt[2], Oliver Jensen[3], Nigel Mottram[4], Dmitri Miroshnychenko[5], Shailesh Naire[6], Raffaella Ocone[6], Jennifer Siggers[3] and Andrew Smith[4].

Abstract

In this report, we consider retinal detachment in the eye, which happens when the retina comes away from the choroid. This condition is often treated by removing the vitreous humour from the eye (vitrectomy) and spot-welding the retina back on to the choroid. After this, the vitreous body is refilled with saline or silicone oil. The vitreous humour is a viscoelastic material, with a very high effective viscosity, and therefore it remains almost stationary relative to the position of the eyeball. However, after the vitrectomy, linear viscous fluid flows will occur in the vitreous body. One post-operative complication that may arise is re-detachment of the retina, which may occur due to increased wall shear stress in a post-vitrectomy eye, caused by the fluid flows.

Two mechanisms have been postulated for these flows:

- The front of the eye is exposed to the cold atmosphere, meaning that the front wall of the posterior chamber will be at a slightly lower temperature than the back wall. The cooler fluid will have a slightly higher density, so it tends to sink, which in turn drives a flow throughout the posterior chamber.

[1]University of Oxford
[2]University of Southampton
[3]University of Nottingham
[4]University of Strathclyde
[5]University of Glasgow
[6]Heriot-Watt University

- The eyeball will move due to head motion, and also due to rotations of the eyeball within its socket (both voluntary and involuntary). These motions drive a flow in the posterior chamber.

We proceed to investigate the nature of flows driven by each of these mechanisms by constructing a simple model in each case. Of particular interest is the wall shear stress generated by the flows, which we estimate in both cases. For the buoyancy-driven flow, we consider the limit of very small temperature differences between the front and the back part. For the eyeball-motion-driven flow, we specialise to a model of saccadic motion of the eye, and consider two special limits: the limit of small rotation angle of the eyeball during the saccadic movement; and the limit of very high-frequency oscillations of the eyeball (also with small amplitudes). In the latter case, a Stokes boundary layer forms at the wall, and a steady streaming flow is generated, which persists into the interior of the eye. We also compare these values with an estimate of the wall shear stress in normal eyes, accounting for the viscoelastic properties of the vitreous. Finally, we model the retina as an elastic layer, and investigate its deformation under a prescribed wall shear stress.

1 Introduction

The condition of retinal detachment (RD) occurs in a human eye when the retina no longer remains in contact with the choroid (the cellular layer between the retina and the sclera). This condition threatens the sight of millions of patients every year and, along with cataracts (which are curable with a relatively simple and cheap operation), is the major cause of sight loss worldwide. Retinal detachments usually happen over a relatively short period of time (a few days or weeks). If the affected patient does not receive treatment rapidly then permanent and incurable blindness will rapidly result.

For various complicated clinical reasons the majority of RDs occur near to the top (north pole) of the eye. Treatments for RD vary widely from laser spot-welding to scleral buckling, but vitrectomy (the removal of the vitreous humour from the posterior segment of the eye) is frequently involved. Under normal circumstances vitreous humour may be thought of as an elastic solid that permits very little flow. After vitrectomy the vitreous is normally replaced by saline (which may or may not include gas to tamponade and thereby reattach the retina) or silicone oil; in either case the posterior segment becomes filled with a fluid that allows normal linear viscous flow to take place. A number of questions now arise concerning possible flows that might take place in this fluid and how such flows might affect post-operative

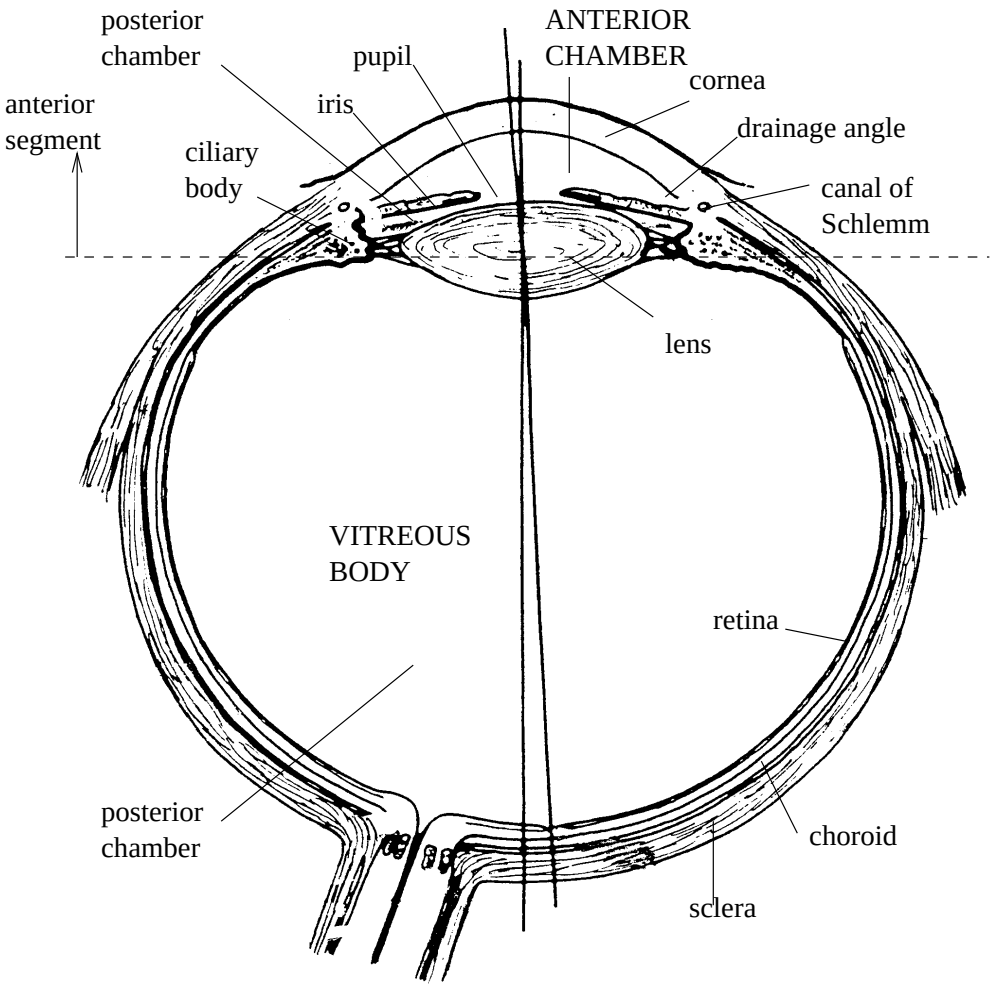

Figure 1: The eye

recovery after RD treatment.

Some have conjectured that flow may be driven by the thermal gradients present in the eye. These buoyancy forces arise from the difference in temperature of the parts of the eye that are exposed to ambient temperature (*i.e.* the thin slit between the eyelids) and the rest of the eye which, being well supplied with blood vessels may be thought of as being held at a constant 37° C. It is known that buoyancy-driven flows of this type occur in other parts of the human body (for example, in the anterior chamber of the eye [3], and in the semi-circular canals of the ear.)

In addition to possible buoyancy-driven flows, so called saccadic motions of the eyes, *i.e.* rapid movements of the head and/or eyeball, will cause fluid flow in the posterior section of the eye. Saccadic motions occur many times

every day for a number of reasons. Some examples are: turning one's head or eyes to look at an object of interest perceived in the peripheral vision; during reading; small amplitude intrusions whilst fixating on an object; the rapid eye movement (REM) that occurs during approximately four periods in a night's sleep; and slow eye movement (SEM) during sleep onset. Less frequently, there may also be more violent causes, such as being struck on the head.

It is clear that both convection and saccadic motion have the potential to cause flow in the posterior segment of the eye, but why is such flow potentially important in a post-vitrectomy patient? The answer lies in the fact that sometimes, a number of days after seemingly successful reattachment surgery (which may involve reattachment using either heat or cryogenics) a subsequent retinal detachment takes place at the top of the eye. It is conjectured that this may be due to the following chain of events: (1) Scar tissue is formed at the sight of the original reattachment (2) Parts of the scar tissue are convected to the bottom of the eye (or perhaps fall there under gravity): note that in the absence of vitrectomy this would be impossible (3) After a few days the scar tissue contracts at the bottom of the eye and this pulls away the retina from the top of the eye.

The subject of this report is therefore to address some or all of the following questions:

1. Is buoyancy-driven flow a realistic possibility?
2. What strength of flow is caused by saccadic eye movements?
3. How large are the forces induced at the retinal wall due to the fluid motion produced by these mechanisms?
4. Can anything be said about the fluid mechanics of such flows?
5. How do the magnitudes of such flows compare to the rate of settling of scar tissue under gravity?
6. Could scar tissue accrete at the bottom of the eye and give rise to the post-operative complications described above?

We shall investigate the possibility of flows in the posterior segment of the eye driven by buoyancy forces and saccadic motions. We study a simple model of the posterior chamber in each case. The fluid flow generated exerts a force per unit area on the retina, the wall shear stress (WSS), and this is the fluid-mechanical force that would be responsible for convecting the scar tissue to the bottom of the eye, and pulling the retina away from the wall.

Thus one of the main aims of these models is to estimate the WSS induced by the flows caused by each of the mechanisms in the post-vitrectomy eye.

For each model, the posterior chamber is approximated by a fluid-filled sphere of radius a, filled with an incompressible fluid of density ρ and kinematic viscosity ν. We use spherical coordinates (r^*, θ, ϕ), and denote the components of the fluid velocity in the coordinate directions by $\mathbf{u}^* = (u^*, v^*, w^*)$, where stars indicate dimensional variables. The WSS produced in the directions of increasing θ and ϕ are given by $\tau^*_\theta = \mu e^*_{r\theta}$ and $\tau^*_\phi = \mu e^*_{\phi r}$ respectively, where

$$e^*_{r\theta} = \frac{1}{2}\, v^*_{r^*}|_{r^*=a}\,, \quad e^*_{\phi r} = \frac{1}{2}\, w^*_{r^*}|_{r^*=a}\,,$$

and μ is the bulk viscosity.

In §2, we consider buoyancy-driven flows, and formulate a model in the case where the patient is supine. We assume that the wall of the posterior chamber is at constant body temperature in the posterior part, and at a cooler constant temperature in the anterior part, due to the fact that the front of the eye is exposed to the cold atmosphere. With this set up, the flow is then governed by three dimensionless parameters: the Rayleigh number, which describes how large the buoyancy forces are relative to viscous forces, the Prandtl number, equal to the kinematic viscosity divided by the thermal diffusivity, and the proportion of the sphere wall at the lower temperature. We estimate the WSS for small Rayleigh numbers, and compare the predicted values of the WSS for physiological parameter values.

Several causes of saccadic motion were given in the introduction. One of these is turning the eyes rapidly to look at an object. This was investigated by Rottach *et al.* [13]. They asked subjects to make saccades between visible targets 20° or 40° apart, and investigated the difference in the eye motion when the subject attempted not to blink, compared with the same exercise accompanied by voluntary blinking. They found that the saccades lasted around 0.1 s, and speeds of $\sim 400^\circ\,\mathrm{s}^{-1}$ were achieved during the motion. The peak velocity and acceleration of the eye during saccades accompanied by blinks were $\sim 20\%$ lower than those without a blink, and hence the duration of the saccades were longer. The probability that the eyes overshot the target also increased in saccades with blinks.

A review of eye movements during reading was given by Liversedge & Findlay [8]. Whilst reading, the eyes repeatedly fixate on different points in the text for durations of 60 to 500 ms. Between fixations there are saccadic movements, which are usually of shorter duration; on average, when reading English text, 85% of these are from left to right. A saccade typically moves the fixation 7–9 characters downstream, although they can be as short as only one character and as long as the length of text (*e.g.* when moving

from one line to the next). In the text, readers tend to fixate on content words, which are usually quite long, but skip function words, which tend to be shorter. Fixations usually land between the beginning and the centre of a word; however, the perceptual span is asymmetric, being extended towards the direction in which the reader progresses through the text. In English it covers about four characters to the left and 15 characters to the right. Bilingual readers, who can read both a left-to-right and a right-to-left language, will switch their perceptual span offset according to the language they are reading. Yang & McConkie [14] measured the saccades made by 36 students during reading, and found that fixations lasted on average 212 ms, and forward saccades covered on average 7.69 characters, whilst regressive saccades spanned 5.93 characters on average. The saccade main sequence [2] implies that the saccade durations are ~ 50 ms.

Abadi & Gowen [1] studied involuntary movements made by the eyes of all fifty of their subjects, while they were attempting to fixate on a single point. They found that the so-called saccadic intrusions fell into four categories, according to the shape of the wave-form; the most frequent were monophasic square wave intrusions (MSWI), which occurred approximately 11.5 times per minute, and had amplitudes $\sim 0.7^\circ$ and durations ~ 225 ms. The speed was up to $150^\circ\,\mathrm{s}^{-1}$ and the acceleration up to $8000^\circ\,\mathrm{s}^{-2}$. Another form of eye motions is the rapid eye movement (REM) whilst sleeping. During REM, the eye movements have a typical amplitude of 5–12° [10]. The maximum velocity attained during a movement is around $50^\circ\,\mathrm{s}^{-1}$, but occasionally is in excess of $200^\circ\,\mathrm{s}^{-1}$. During the onset of sleep, the eyes also make slow drifting or rolling movements, called slow eye movement (SEM), which was studied by Porte [10]. These typically have amplitude $\sim 10^\circ$, period ~ 2 s and maximum speed $\sim 20^\circ\,\mathrm{s}^{-1}$.

In §3, we study a simple model of saccadic motion of the eye. We model the posterior chamber of the eye as a hollow sphere of radius a, filled with a fluid of viscosity ν, and assume that the wall of the chamber performs torsional oscillations about the vertical axis of amplitude ϵ and frequency ω. The corresponding Womersley number is $\alpha = \sqrt{a^2\omega/\nu}$, which is equal to the square root of the frequency multiplied by the viscous timescale across the sphere. David *et al.* [4] also considered torsional oscillations of a hollow sphere, filled with a viscoelastic fluid, and solved this in the asymptotic limit in which the oscillations have small amplitude. The solution is found in terms of modified spherical Bessel functions and represents a quasi-steady perturbation about a rigid body oscillation.

A similar fluid dynamical problem was studied by Riley [11], who provided a review of the work done on flows around a solid body that is performing translational oscillations of velocity $U_\infty \cos \omega t^*$ in an infinite fluid bath of

viscosity ν, that is otherwise at rest. The nondimensional flow is governed by ϵ and $\alpha = \sqrt{a^2\omega/\nu}$, where in this case, a is a typical lengthscale of the body. It is possible to make analytical progress in the limit $\epsilon \to 0$; at leading order in this limit, the dominant balance is between the time-dependent inertia term and the viscous term, giving velocities proportional to $\cos t$, where $t = \omega t^*$ is the nondimensional time. At next order, the convective inertia terms contain components proportional to $\cos^2 t = (1 + \cos 2t)/2$, giving rise to a steady streaming contribution to the solution. This steady streaming has an associated Reynolds number, $R_s = U_\infty^2/\omega\nu = \epsilon^2\alpha^2$, whilst the conventional Reynolds number of the flow generated by the body is $R = U_\infty a/\nu = \epsilon\alpha^2$. Analytical progress may be made in three cases: (i) $\alpha = O(1)$ and $R, R_s \ll 1$, (ii) $R = O(1)$, $R_s \ll 1$ and $\alpha \gg 1$ and (iii) $R_s = O(1)$ and $R, \alpha \gg 1$ (the study done in [4] corresponds to case (i)). A matched asymptotic expansion technique was used to develop a theory in each of these cases.

Lyne [9] also investigated flows driven by oscillatory forces. He considered the fully-developed flow through a weakly curved pipe, driven by an oscillatory pressure gradient. He developed an asymptotic theory in the limit of large Womersley number (equivalent to case (iii) above), and found that in this limit a Stokes boundary layer is formed around the edges of the pipe. The oscillations in the boundary layer have a non-zero mean, which is caused by the effects of the centrifugal force. The mean flow drives a large-scale steady secondary streaming flow across the interior of the pipe. This secondary flow is governed by a streaming Reynolds number R_s. Lyne proceeded to find the asymptotic form of the solution for both small and large values of R_s.

The fluid motion induced by torsional oscillations of a sphere in an infinite body of fluid was studied analytically by Gopinath [5] and reviewed by Riley [12]. They showed that for high Womersley numbers, a thin Stokes layer is formed at the surface of the sphere, and steady streaming persists beyond it. The streaming consists of movement of the fluid from the poles of the sphere to the equator. For large values of R_s, a radial jet of fluid is ejected at the equator. This system was also investigated experimentally and numerically in [6] for large Womersley numbers. The experimental observations showed that the flow is nearly axisymmetric and is also symmetric in the plane of the equator. A Stokes boundary layer is formed at the surface of the sphere, which gives rise to a radial jet in the equatorial plane. The speed of the jet fluctuates, and as the oscillation amplitude is increased, the fluctuations become progressively larger until the faster parts of the jet overtake the slower ones, causing them to curl back on themselves, forming vortex pairs. However, there are no detailed studies of the steady streaming flow *inside* an oscillating sphere.

In §3.2, we estimate the WSS for $\alpha = O(1)$, and also for $\alpha \gg 1$, when a

boundary layer forms at $r^* = a$. We then proceed to solve the full Navier–Stokes equations for the fluid flow in the sphere. In the subsequent sections, we look at the structure of the fluid flows in the vitreous body, considering two cases in particular: $\epsilon \ll 1$ and $\alpha = O(1)$, considered in §3.3, and $\alpha \gg \epsilon^{-1} \gg 1$, which is considered in §3.4. In both cases, we find the leading order part of the fluid velocity. Then, in §3.5, we perform a similar calculation to find the WSS in a normal, rather than post-vitrectomy, eye, following [4]. We model the vitreous humour as a Maxwell-Kelvin viscoelastic material [7], and for small amplitude oscillations follow a similar solution procedure to determine the approximate WSS.

In §4, we discuss a model of the shear-stress-induced mechanism of detachment of the retina. We write down model equations governing the behaviour of a weakly-attached portion of the retina that is under a prescribed WSS, arising from the fluid motion, and use them to predict the deformation of the retina in the weakly-attached region.Finally in §5, we discuss all the results, and compare the values of the WSS induced by buoyancy forces and saccadic motion.

2 Estimate of wall shear stress induced by buoyancy-driven flow in the eye

There is a temperature gradient across the interior of the eye, due to the fact that the front of the eye is exposed to the atmosphere and therefore the anterior boundary of the fluid in the posterior chamber is at a lower temperature than the posterior part, which is at body temperature. In turn, this may give rise to a buoyancy-driven flow which could be important for the RD. We approximate the posterior chamber by a sphere, and consider the set up shown in figure 2. We assume that the anterior part of the wall, for $0 \leq \theta < \theta_0$, is held at a constant temperature, T_0, whilst the posterior section, for $\theta_0 < \theta \leq \pi$, being well supplied with blood vessels, is at the constant higher body temperature, $T_1 = T_0 + \Delta_T$. We further assume that the patient is supine.

We use spherical coordinates (r^*, θ, ϕ) as shown in figure 2, and use the Boussinesq approximation to write the Navier-Stokes equation, the heat equation and the continuity equation in the form

$$\begin{aligned} \mathbf{u}_t^* + (\mathbf{u}^* \cdot \boldsymbol{\nabla}^*)\,\mathbf{u}^* + \rho^{-1}\boldsymbol{\nabla}^* p^* &= \alpha_T g\,(T^* - T_0)\,(\cos\theta \hat{\mathbf{e}}_r - \sin\theta \hat{\mathbf{e}}_\theta) + \nu \nabla^{*2}\mathbf{u}^*, \\ T_t^* + \mathbf{u}^* \cdot \boldsymbol{\nabla}^* T^* &= \kappa \nabla^{*2} T^*, \\ \boldsymbol{\nabla}^* \cdot \mathbf{u}^* &= 0, \end{aligned}$$

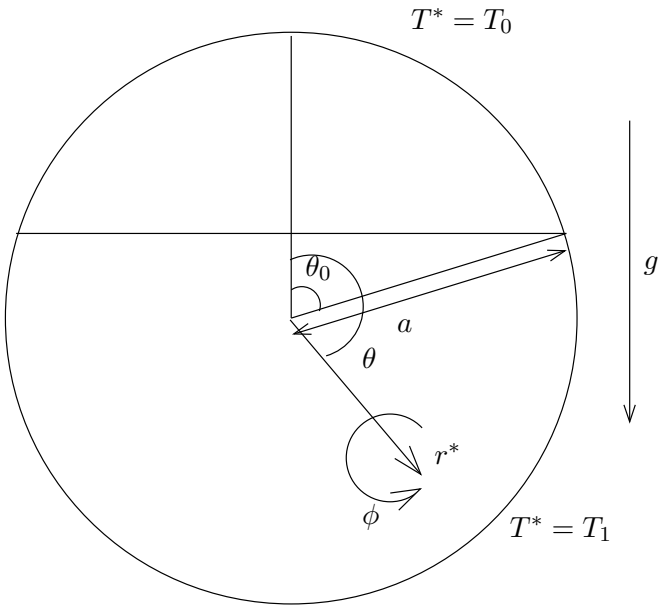

Figure 2: Schematic diagram showing the set up used to estimate the buoyancy-driven flow in the eye.

where T^* is the temperature, κ is the thermal diffusivity, α_T is the coefficient of thermal expansion and g is the acceleration due to gravity, together with no-slip boundary conditions for the $\mathbf{u}^*$ and the boundary conditions on the temperature.

We nondimensionalise by rescaling lengths with a, velocities with κ/a, times with a^2/κ, pressures with $\rho\kappa^2/a^2$ and setting $T^* = T_0 + \Delta_T T$. This yields the equations

$$\mathbf{u}_t + (\mathbf{u}\cdot\boldsymbol{\nabla})\,\mathbf{u} + \boldsymbol{\nabla} p = \sigma R T\,(\cos\theta\hat{\mathbf{e}}_r - \sin\theta\hat{\mathbf{e}}_\theta) + \sigma\nabla^2\mathbf{u}, \tag{1}$$

$$T_t + \mathbf{u}\cdot\boldsymbol{\nabla} T = \nabla^2 T, \tag{2}$$

$$\boldsymbol{\nabla}\cdot\mathbf{u} = 0, \tag{3}$$

where $R = a^3\alpha_T g\Delta_T/\nu\kappa$ is the Rayleigh number, and $\sigma = \nu/\kappa$ is the Prandtl number. The boundary conditions at $r = 1$ are $\mathbf{u} = 0$, $T = 0$ for $0 < \theta \leq \theta_0$ and $T = 1$ for $\theta_0 < \theta \leq \pi$.

We consider the limit $R \ll 1$, in which case we expect that (except in the special cases when θ_0 is close to 0 or π) the fluid flow will be a poloidal field, as shown in figure 3. Thus the solution is steady with no boundary layers, axisymmetric (*i.e.* independent of ϕ) and has $w \equiv 0$. Therefore τ^*_ϕ is zero. To find τ^*_θ, we balance the buoyancy and viscous terms in equation (1) to give $\|\mathbf{u}\| \sim R$, meaning that $\tau^*_\theta \sim \mu\kappa R/a^2$.

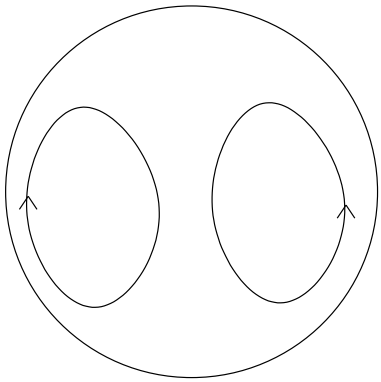

Figure 3: Sketch of the predicted form of the buoyancy-driven fluid motion in the eye for $R \ll 1$.

For the post-vitrectomy eye, we assume that the fluid in the posterior chamber has similar properties to water at 40° C and take

$$\rho = 9.9 \times 10^2 \,\mathrm{kg\,m^{-3}}, \quad \nu = 6.8 \times 10^{-7} \,\mathrm{m^2\,s^{-1}}, \quad \alpha_T = 3.9 \times 10^{-4} \,\mathrm{K^{-1}},$$
$$\kappa = 1.5 \times 10^{-7} \mathrm{m^2\,s^{-1}} \quad g = 9.8 \,\mathrm{m\,s^{-2}} \text{ and } \quad a = 1.1 \times 10^{-2} \,\mathrm{m}.$$

This gives $R = 5.0 \times 10^4 \Delta_T$, where Δ_T is measured in K, and $\sigma = 4.3$; unfortunately it is not possible easily to estimate Δ_T. If we assume we are in the $R \ll 1$ regime, then $\tau_\theta^* \sim 0.04 \Delta_T \,\mathrm{kg\,m^{-1}\,s^{-2}}$.

We do expect Δ_T to be fairly small, since most of the temperature difference will occur across the anterior chamber, leaving only a small temperature difference in the posterior [3]. However, it seems unlikely that Δ_T is sufficiently small that we are truly in the $R \ll 1$ regime. We do know for certain that Δ_T must be less than the difference between body temperature and the atmospheric temperature, and so $\Delta_T \lesssim 37 - 20 = 17 \,\mathrm{K}$. Thus $R \lesssim 9 \times 10^5$; this upper bound corresponds to the "worst case" estimate for τ_θ^*, which is $0.7 \,\mathrm{kg\,m^{-1}\,s^{-2}}$.

3 Fluid motion due to eye movement

3.1 Introduction

In the previous section, we estimated the WSS due to buoyancy-driven fluid motion. However, as mentioned in the introduction, saccadic eye-motion will also cause the fluid to move, and exert a WSS. In this section, we use a simple model to estimate the WSS due to these motions, and also solve the Navier–Stokes equations explicitly to find the fluid flow in certain parameter

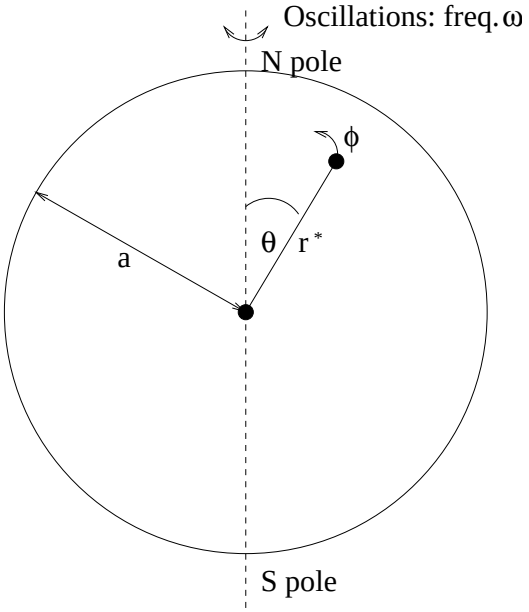

Figure 4: Schematic diagram of the eye performing torsional oscillations, showing the coordinate system used.

regimes. We model the saccadic motions as oscillations of frequency ω and amplitude ϵ about a vertical axis, see figure 4. The fluid flow is then governed by the amplitude, ϵ, and Womersley number, α. We now estimate the sizes of these two parameters in the post-vitrectomy eye during the various everyday activities discussed above. We take $a \approx 1.1\,\mathrm{cm}$ [4] and ν to be the kinematic viscosity of water at $40^\circ\,C$, *i.e.* $6.8\times10^{-7}\,\mathrm{m^2\,s^{-1}}$. Upon calculating the values of ϵ and α for the activities mentioned earlier, which are given in table 1 on page 28, we see that the values of ϵ are quite small, whilst α tends be large. This motivates considering the following cases:

- Case I: we assume that $\epsilon \ll 1$ and $\alpha = O(1)$. This corresponds to case (i) by Riley mentioned above. When α is large, we find that the non-zero velocities become confined to a boundary layer near the wall, motivating case II;

- Case II: we assume $\alpha \gg \epsilon^{-1} \gg 1$. In this case, we obtain a Stokes boundary layer of thickness α^{-1}, which gives rise to steady secondary streaming. The streaming solution penetrates into the interior of the sphere, causing a large-scale steady flow throughout the sphere.

We use the coordinate system pictured in figure 4, with coordinates (r^*, θ, ϕ), where stars denote dimensional variables and coordinates. If the corresponding fluid velocity components are denoted $\mathbf{u}^* = (u^*, v^*, w^*)$, then the no-slip boundary conditions become $u^* = v^* = 0$, $w^* = \epsilon a\omega \sin\theta \sin\omega t^*$ on $r^* = a$. We nondimensionalise lengths with respect to a, velocities with respect to $a\omega$, pressures with respect to $\rho a^2\omega^2$ and time with respect to ω^{-1}. The Navier–Stokes equations become

$$\mathbf{u}_t + \mathbf{u}\cdot\boldsymbol{\nabla}\mathbf{u} = -\boldsymbol{\nabla}p + \frac{1}{\alpha^2}\nabla^2\mathbf{u}, \quad \boldsymbol{\nabla}\cdot\mathbf{u} = 0,$$

subject to the boundary conditions $u = v = 0$, $w = \epsilon\sin\theta\sin t$ at $r = 1$. Assuming that the solution is axisymmetric, the equations become

$$u_t + uu_r + \frac{vu_\theta}{r} - \frac{v^2}{r} - \frac{w^2}{r} = -p_r + \frac{1}{\alpha^2}\left(\nabla^2 u - \frac{2u}{r^2} - \frac{2(v\sin\theta)_\theta}{r^2\sin\theta}\right), \tag{4}$$

$$v_t + uv_r + \frac{vv_\theta}{r} + \frac{uv}{r} - \frac{w^2\cot\theta}{r} = -\frac{p_\theta}{r} + \frac{1}{\alpha^2}\left(\nabla^2 v + \frac{2u_\theta}{r^2} - \frac{v}{r^2\sin^2\theta}\right), \tag{5}$$

$$w_t + uw_r + \frac{vw_\theta}{r} + \frac{uw}{r} + \frac{vw\cot\theta}{r} = \frac{1}{\alpha^2}\left(\nabla^2 w - \frac{w}{r^2\sin^2\theta}\right), \tag{6}$$

$$\frac{(r^2u)_r}{r^2} + \frac{(v\sin\theta)_\theta}{r\sin\theta} = 0. \tag{7}$$

We may also introduce a streamfunction, ψ, via

$$u = \frac{\psi_\theta}{r^2\sin\theta}, \quad v = -\frac{\psi_r}{r\sin\theta}. \tag{8}$$

This enables the system (4)–(7) to be reduced to two equations in the variables ψ and w: the azimuthal component of the vorticity equation, which is fourth order in ψ, and the azimuthal component of the Navier–Stokes equation (6). The boundary conditions become $\psi = \psi_r = 0$, $w = \epsilon\sin\theta\sin t$ at $r = 1$. However, for most of this section, it will be more straightforward to use the full system (4)–(7).

3.2 Estimate of the wall shear stress in post-vitrectomy eyes

We now estimate the WSS in this system in the two cases I and II.

In case I, we expect there to be no boundary layers, and the leading order balance to be between the time-derivative and viscous terms in (6).

Together with the boundary condition on w, this gives $w = O(\epsilon)$, and thus $\tau_\phi^* = \mu\omega w_r|_{r=1} \sim \mu\omega\epsilon$, *i.e.* proportional to the maximum speed of the eyeball. To find τ_θ^*, we balance the time-derivative and centrifugal force terms in (4) and (5) to give $u \sim v = O(\epsilon^2)$ and hence $\tau_\theta^* = \mu\omega v_r|_{r=1} \sim \mu\omega\epsilon^2$. Thus, as might be expected, the azimuthal component of WSS is much larger than the zenithal component.

In case II, we assume that a boundary layer of thickness δ forms at $r = 1$, in which the radial derivatives are of order δ^{-1}. In equation (6), we balance the time-derivative and viscous terms to give $w \sim w/\alpha^2\delta^2$, which implies that $\delta \sim \alpha^{-1}$. Coupled with the boundary conditions on w, this means that $\tau_\phi^* \sim \mu\omega\epsilon\alpha$. In equation (5), we balance the time-derivative and centrifugal terms to give $v \sim \epsilon^2$ (and hence from (4), we get $u \sim \epsilon^2\alpha$), meaning that $\tau_\theta^* \sim \mu\omega\epsilon^2\alpha$. Here also, the azimuthal component of the WSS is greater, and both components grow as $\omega^{3/2}$ for large ω.

3.3 Fluid dynamics in post-vitrectomy eyes. Case I: $\epsilon \ll 1$, $\alpha = O(1)$

In this section, we solve equations (4)–(7) in the limit of small amplitude oscillations. We seek a series solution of the form

$$u = \epsilon^2 u_1 + \epsilon^4 u_2 + \dots, \quad v = \epsilon^2 v_1 + \epsilon^4 v_2 + \dots,$$
$$w = \epsilon w_1 + \epsilon^3 w_2 + \epsilon^5 w_3 + \dots, \quad p = \epsilon^2 p_1 + \epsilon^4 p_2 + \dots,$$

At leading order, $O(\epsilon)$, we obtain the equation

$$\alpha^2 w_{1t} = \nabla^2 w_1 - \frac{w_1}{r^2 \sin^2\theta}, \tag{9}$$

for the meridional flow, which has the solution

$$w_1 = \mathrm{Im}\left(f(r)e^{\mathrm{i}t}\right)\sin\theta$$

after [4], where

$$f(r) = \frac{e^{\sqrt{\mathrm{i}}\alpha r}(1-\sqrt{\mathrm{i}}\alpha r) - e^{-\sqrt{\mathrm{i}}\alpha r}(1+\sqrt{\mathrm{i}}\alpha r)}{r^2(e^{\sqrt{\mathrm{i}}\alpha}(1-\sqrt{\mathrm{i}}\alpha) - e^{-\sqrt{\mathrm{i}}\alpha}(1+\sqrt{\mathrm{i}}\alpha))}. \tag{10}$$

Figures 5(a) and (b) show representative graphs of the real and imaginary parts of f for small and large α. We see that for small α, the fluid moves as a solid body, but as α increases, the fluid flow becomes confined to a boundary layer at $r = 1$. As discussed in the introduction, this is a Stokes boundary layer; we calculate its asymptotic form in the next section.

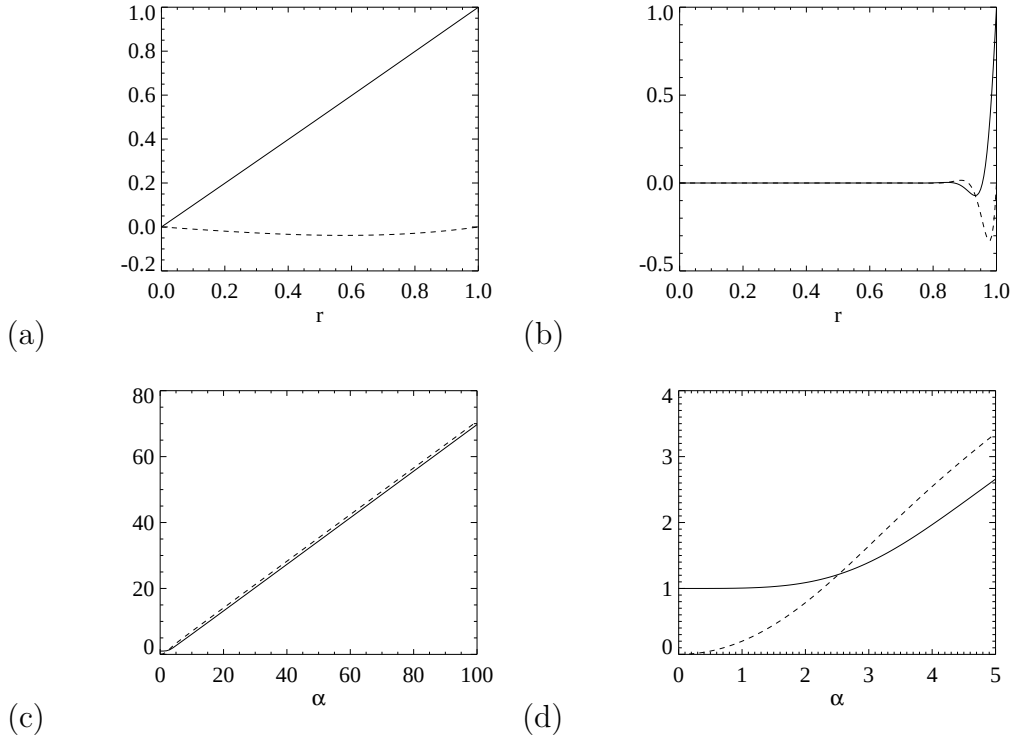

Figure 5: Graphs of the real (solid) and imaginary (dashed) components of f for (a) $\alpha = 1$, (b) $\alpha = 50$. (c) Graph of the real (solid) and imaginary (dashed) components of $f_r|_{r=1}$; (d) enlarged portion of (c) near $\alpha = 0$.

The leading order contribution to the WSS is

$$\frac{1}{2}\mu\omega\epsilon\,\mathrm{Im}\left(f_r|_{r=1}e^{\mathrm{i}t}\right)\sin\theta. \tag{11}$$

Graphs of $f_r|_{r=1}$ against α are shown in figure 5. For $\alpha \ll 1$, $f(r) = r + O(\alpha^2)$, and so

$$\tau_\phi^* = \frac{1}{2}\mu\omega\epsilon\sin t\sin\theta\left(1+O(\alpha^2)\right), \tag{12}$$

agreeing with the estimate in §3.2, whilst for $\alpha \gg 1$,

$$f(r) = e^{\sqrt{\mathrm{i}}\alpha(r-1)}\frac{1-\sqrt{\mathrm{i}}\alpha r}{r^2(1-\sqrt{\mathrm{i}}\alpha)}\left(1+O(e^{-\sqrt{2}\alpha r})\right),$$

and thus

$$\begin{aligned}\tau_\phi^* =& \frac{1}{2}\mu\omega\epsilon\mathrm{Re}\left(\frac{\mathrm{i}\alpha^2 - 2\sqrt{\mathrm{i}}\alpha + 2}{\sqrt{\mathrm{i}}\alpha - 1}e^{\mathrm{i}t}\right)\sin\theta\left(1+O(e^{-\sqrt{2}\alpha})\right),\\ \sim& \frac{1}{2}\mu\omega\epsilon\alpha\sin\theta\sin\left(t+\frac{\pi}{4}\right)\left(1+O\left(\frac{1}{\alpha}\right)\right),\end{aligned} \tag{13}$$

also agreeing with the estimate in §3.2.

At $O(\epsilon^2)$, equations (4)–(7) become

$$\begin{aligned} u_{1t} - \frac{w_1^2}{r} &= -p_{1r} + \frac{1}{\alpha^2}\left(\nabla^2 u_1 - \frac{2u_1}{r^2} - \frac{2(v_1\sin\theta)_\theta}{r^2\sin\theta}\right),\\ v_{1t} - \frac{w_1^2\cot\theta}{r} &= -\frac{p_{1\theta}}{r} + \frac{1}{\alpha^2}\left(\nabla^2 v_1 + \frac{2u_{1\theta}}{r^2} - \frac{v_1}{r^2\sin^2\theta}\right),\\ \frac{(r^2u_1)_r}{r^2} + \frac{(v_1\sin\theta)_\theta}{r\sin\theta} &= 0,\end{aligned}$$

which we cannot solve analytically. However, these equations show that if u_1 and v_1 were both identically zero, then the pressure field, p_1, would need to balance the centrifugal terms. However, since $(w_1^2/r)_\theta \neq (w_1^2\cot\theta/r)_r$, this is not possible, and we conclude that a 3D flow must be generated. We now explore this 3D flow in the case when α is large enough for the flow to have a boundary layer structure, which we shall consider in the next section.

3.4 Fluid dynamics in post-vitrectomy eyes. Case II: $\alpha \gg \epsilon^{-1} \gg 1$

In the Stokes layer, we set $r = 1 - \eta/\alpha$, where η is $O(1)$, and substitute

$$u = \frac{1}{\alpha}u_0 + O\left(\frac{1}{\alpha^2}\right), \quad v = v_0 + O\left(\frac{1}{\alpha}\right), \quad w = w_0 + O\left(\frac{1}{\alpha}\right),$$
$$p = p_0 + \frac{1}{\alpha}p_1 + O\left(\frac{1}{\alpha^2}\right).$$

At $O(\alpha^{-1})$, equation (4) implies that

$$p_{0\eta} = 0, \tag{14}$$

and at $O(1)$, equations (5)–(7) become

$$v_{0t} - u_0 v_{0\eta} + v_0 v_{0\theta} - w_0^2 \cot\theta = -p_{0\theta} + v_{0\eta\eta}, \tag{15}$$
$$w_{0t} - u_0 w_{0\eta} + v_0 w_{0\theta} + v_0 w_0 \cot\theta = w_{0\eta\eta}, \tag{16}$$
$$-u_{0\eta} + v_{0\theta} + v_0 \cot\theta = 0, \tag{17}$$

together with the boundary conditions $u_0 = v_0 = 0$ and $w_0 = \epsilon \sin t \sin\theta$. We can solve (15)–(17) as a series solution in powers of ϵ, by writing

$$u_0 = \epsilon^2 u_{00} + \epsilon^4 u_{01} + \ldots, \quad v_0 = \epsilon^2 v_{00} + \epsilon^4 v_{01} + \ldots,$$
$$w_0 = \epsilon w_{00} + \epsilon^3 w_{01} + \ldots, \quad p_0 = \epsilon^2 p_{00} + \epsilon^4 p_{01} + \ldots.$$

At leading order,

$$p_{00\eta} = 0, \quad v_{00t} - w_{00}^2 \cot\theta = -p_{00\theta} + v_{00\eta\eta},$$
$$w_{00t} = w_{00\eta\eta}, \quad -u_{00\eta} + v_{00\theta} + v_{00}\cot\theta = 0,$$

which has the solution

$$\begin{aligned}
u_{00} =&\frac{1}{16\sqrt{2}}\left(e^{-\sqrt{2}\eta}\left(\cos\left(2t-\sqrt{2}\eta\right)-\sin\left(2t-\sqrt{2}\eta\right)\right)\right.\\
&-\sqrt{2}e^{-\eta}\left(\cos\left(2t-\eta\right)-\sin\left(2t-\eta\right)\right)+\left(\sqrt{2}-1\right)\left(\cos 2t-\sin 2t\right)\\
&\left.+2\sqrt{2}\eta+2e^{-\sqrt{2}\eta}-2+\sqrt{2}A\eta^2\right)\left(3\cos 2\theta+1\right)\\
&+\left(\frac{B\eta^2}{2}+\frac{\eta^3}{6}\right)\left(f''(\theta)+f'(\theta)\cot\theta\right), \qquad (18)\\
v_{00} =&\frac{1}{8}\left(e^{-\sqrt{2}\eta}\sin\left(2t-\sqrt{2}\eta\right)-e^{-\eta}\sin\left(2t-\eta\right)-e^{-\sqrt{2}\eta}+1+A\eta\right)\sin 2\theta\\
&+\left(B\eta+\frac{\eta^2}{2}\right)f'(\theta), \qquad (19)\\
w_{00} =&e^{-\eta/\sqrt{2}}\sin\left(t-\frac{\eta}{\sqrt{2}}\right)\sin\theta, \qquad (20)\\
p_{00} =&f(\theta), \qquad (21)
\end{aligned}$$

where A and B are unknown constants and f is an unknown function. The solution w_{00} is the usual Stokes layer solution; the nonlinear centrifugal forces from this solution generate zenithal flow v_{00}. This flow is not proportional to $1/\sin\theta$, and so to satisfy continuity, it ejects a radial flow u_{00}. As we come to the edge of the boundary layer, setting $\eta\sim O(\alpha)$, we find that

$$\begin{aligned}
u \sim&\frac{\epsilon^2}{16\sqrt{2}}\left(\sqrt{2}\alpha A(1-r)^2\left(3\cos 2\theta+1\right)\right.\\
&\left.+\left(\frac{1}{2}B\alpha(1-r)^2+\frac{1}{6}\alpha^2(1-r)^3\right)\left(f''(\theta)+f'(\theta)\cot\theta\right)+O(1)\right),\\
v \sim&\frac{\epsilon^2}{8}\left(A\alpha(1-r)\sin 2\theta+\left(B\alpha(1-r)+\frac{1}{2}\alpha^2(1-r^2)\right)f'(\theta)+O(1)\right).
\end{aligned}$$

Thus $A=0$, and $f(\theta)$ should be a constant function in order to avoid the generation of large velocities in the interior of the sphere. We assume this to be the case, though it should be checked *a posteriori* by matching to the flow in the interior.

The Stokes streamfunction corresponding to the solution (18)–(21) is

$$\psi=\frac{\epsilon^2}{\alpha}\psi_{00}+O\left(\frac{\epsilon^4}{\alpha},1\right),$$

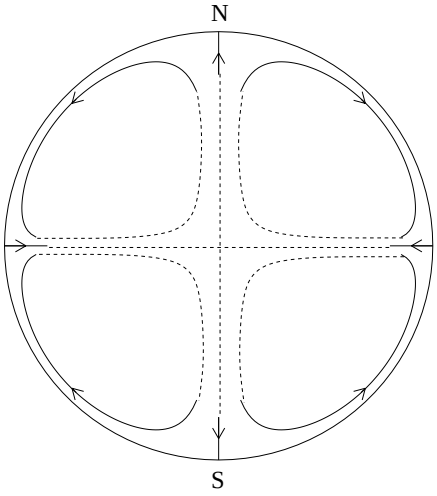

Figure 6: The leading order part of the streaming solution in the Stokes boundary layer. The dashed curves indicate the qualitative prediction of the streaming flow in the interior of the sphere.

where

$$\psi_{00} = \frac{1}{32\sqrt{2}}\left(e^{-\sqrt{2}\eta}\left(\cos\left(2t-\sqrt{2}\eta\right)-\sin\left(2t-\sqrt{2}\eta\right)\right)\right.$$
$$-\sqrt{2}e^{-\eta}\left(\cos\left(2t-\eta\right)-\sin\left(2t-\eta\right)\right)+\left(\sqrt{2}-1\right)\left(\cos 2t-\sin 2t\right)$$
$$\left.+2\sqrt{2}\eta+2e^{-\sqrt{2}\eta}-2\right)\left(\cos\theta-\cos 3\theta\right).$$

Figure 6 shows the streamlines of the steady component of ψ in the boundary layer.

The components of the WSS induced by the solution (18)–(21) are

$$\tau_\phi^* = \mu\omega e_{\phi r} = \frac{\mu\omega\epsilon\alpha}{2}\sin\left(t+\frac{\pi}{4}\right)\sin\theta, \tag{22}$$

$$\tau_\theta^* = \mu\omega e_{r\theta} = \frac{\mu\omega\epsilon^2\alpha}{16}\left(\left(2-\sqrt{2}\right)\sin\left(2t+\frac{\pi}{4}\right)-\sqrt{2}\right)\sin 2\theta, \tag{23}$$

and so the largest stress is achieved at the equator at $t = \pi/4$. This agrees with both the estimate in §3.2 and also with the large-α behaviour in equation (13).

As η becomes large, the exponentially decaying parts of the solution decay

rapidly, leaving

$$u_0 \sim \frac{\epsilon^2}{8\sqrt{2}}\left(\sqrt{2}\eta - 1\right)(3\cos 2\theta + 1) + O(\epsilon^4), \tag{24}$$

$$v_0 \sim \frac{\epsilon^2}{8}\sin 2\theta + O(\epsilon^4), \tag{25}$$

$$w_0 \sim O(\epsilon^3), \tag{26}$$

$$p_0 \sim O(\epsilon^4), \tag{27}$$

which is steady to leading order. Thus, even though the leading order part of the flow, $w \sim \epsilon w_{00}$, decays away from the boundary, the centrifugal forces generate a streaming solution, which persists into the interior of the sphere.

To solve for the flow in the interior, we must match the behaviour with the asymptotic behaviour (24)–(27). However, since u_0 grows linearly with η, the series solution will break down if $\eta \sim O(\epsilon^{-1})$, since the convective inertia now appears in the equations (14)–(17) at leading order. We set $\eta = \epsilon^{-1}\hat{r}$, and seek the solution in the region where $\hat{r}$ is $O(1)$. The large-η behaviour of (24)–(27) motivates us to try setting

$$u_0 = \epsilon\hat{u}(\hat{r},\theta), \quad v_0 = \epsilon^2\hat{v}(\hat{r},\theta), \quad w_0 = 0, \quad p_0 = \epsilon^4\hat{p}(\hat{r},\theta),$$

and, with this assumption, equations (14), (15) and (17) become

$$0 = \hat{p}_{\hat{r}}, \tag{28}$$

$$-\hat{u}\hat{v}_{\hat{r}} + \hat{v}\hat{v}_\theta = -\hat{p}_\theta + \hat{v}_{\hat{r}\hat{r}}, \tag{29}$$

$$-\hat{u}_{\hat{r}} + \hat{v}_\theta + \hat{v}\cot\theta = 0. \tag{30}$$

The behaviour when $\hat{r} \ll 1$ can be determined from matching with (24)–(27) to give

$$\hat{u} \sim -\frac{\hat{r}}{8}(3\cos 2\theta + 1), \quad \hat{v} \sim -\frac{1}{8}\sin 2\theta.$$

Unfortunately, it is not possible to solve equations (28)–(30) analytically, but when $\hat{r} \gg 1$, we assume that the leading order balance is between the convective inertia terms and the pressure gradient. This implies that for $\hat{r} \gg 1$, we have $\hat{p} = O(1)$, and hence $\hat{v} = O(1)$ and $\hat{u} \sim \hat{r}$. Thus at the edge of this boundary layer ($\hat{r} \sim \epsilon\alpha$), we have $u \sim \epsilon^2$, $v \sim \epsilon^2$ and $p \sim \epsilon^4$, which motivates setting $u = \epsilon^2\tilde{u}(r,\theta)$, $v = \epsilon^2\tilde{v}(r,\theta)$, $w = 0$, $p = \epsilon^4\tilde{p}(r,\theta)$ in the core. Upon substitution into equations (4)–(7), we get equations for the leading

order steady streaming component of the solution in the core, which are

$$\tilde{u}\tilde{u}_r + \frac{\tilde{v}\tilde{u}_\theta}{r} - \frac{\tilde{v}^2}{r} = -\tilde{p}_r, \tag{31}$$

$$\tilde{u}\tilde{v}_r + \frac{\tilde{v}\tilde{v}_\theta}{r} + \frac{\tilde{u}\tilde{v}}{r} = -\frac{\tilde{p}_\theta}{r}, \tag{32}$$

$$\frac{(r^2\tilde{u})_r}{r^2} + \frac{(\tilde{v}\sin\theta)_\theta}{r\sin\theta} = 0. \tag{33}$$

Again, it is not possible to solve these equations analytically. However, this behaviour permits us to comment on the case $\epsilon = O(1)$. In this case, the system (14)–(17) gives the scalings $u_0 \sim \eta$, $v_0 \sim 1$, $w \ll 1$ and $p_0 \sim 1$ for $\eta \gg 1$. Thus at the edge of the boundary layer ($\eta \sim \alpha^{-1}$), we have $u \sim v \sim p \sim 1$ and so we predict that equations (31)–(33) will also give the leading order behaviour of the streaming component of the solution in the core in this case. Therefore, the streaming solution has velocities of magnitude $O(1)$.

In summary, the oscillatory azimuthal driving motion of the boundary gives rise to a corresponding azimuthal flow in the boundary layer. The resulting centrifugal forces produce a steady streaming flow in the zenithal direction towards the equator. This in turn means that fluid has to be radially ejected from the equator into the interior of the sphere, and also injected from the interior towards the poles. In turn, this sets up a large-scale streaming throughout the interior of the sphere, see figure 6, with velocities of magnitude $O(\epsilon^2)$.

3.5 Fluid dynamics in normal eyes: $\epsilon \ll 1$

Following Lee *et al.* [7], we model the vitreous humour as an isotropic viscoelastic fluid whose behaviour under shear is modelled by a Maxwell element with modulus μ_m and viscosity η_m in series with a Kelvin element with modulus μ_k and viscosity η_k, as shown in figure 7. The spring and dashpot constants are given by

$$\mu_\mathrm{m} = 3.02\,\mathrm{kg\,m^{-1}\,s^{-2}}, \quad \mu_\mathrm{k} = 1.21\,\mathrm{kg\,m^{-1}\,s^{-2}},$$
$$\eta_\mathrm{m} = 4.86\,\mathrm{kg\,m^{-1}\,s^{-1}}, \quad \eta_\mathrm{k} = 0.49\,\mathrm{kg\,m^{-1}\,s^{-1}},$$

and we take the density to be $1000\,\mathrm{kg\,m^{-3}}$. The total dimensional stress, σ, and strain, e, are given by

$$\sigma = \sigma_1 = \sigma_2 = \sigma_3 + \sigma_4, \quad e = e_1 + e_2 + e_3, \quad e_3 = e_4, \tag{34}$$

$$\sigma_1 = \omega\eta_\mathrm{m}\dot{e}_1, \quad \sigma_2 = \mu_\mathrm{m}e_2, \quad \sigma_3 = \omega\eta_\mathrm{k}\dot{e}_3, \quad \sigma_4 = \mu_\mathrm{k}e_4, \tag{35}$$

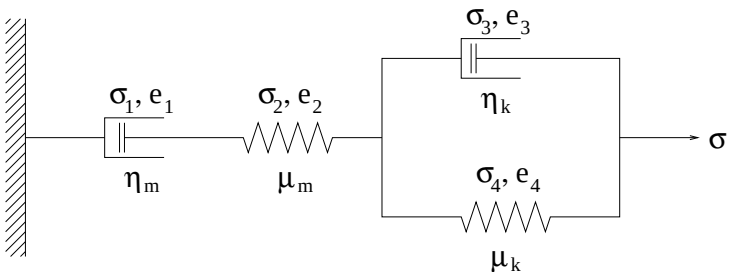

Figure 7: Schematic diagram showing the model of the viscoelastic behaviour of the vitreous humour under shear.

where the σ_i and e_i are the dimensional stresses and strains across the individual components, as indicated in figure 7. We assume that for small amplitudes, the leading contributions to the strain and stress have the same frequency as the oscillations. Thus, working in complex variables, the stresses and strains are given by $\sigma_i = \hat{\sigma}_i e^{\mathrm{i}t}$ and $e_i = \hat{e}_i e^{\mathrm{i}t}$, where $\hat{\sigma}_i$ and $\hat{e}_i$ are independent of time. Substituting these expressions into equations (34)–(35) gives $\sigma = \overline{\mu} e$, where the complex shear modulus $\overline{\mu}$ is given by

$$\overline{\mu} = \left(\frac{1}{\mathrm{i}\omega\eta_\mathrm{m}} + \frac{1}{\mu_\mathrm{m}} + \frac{1}{\mu_\mathrm{k} + \mathrm{i}\omega\eta_\mathrm{k}} \right)^{-1} = \overline{\mu}_\mathrm{r} + \mathrm{i}\overline{\mu}_\mathrm{i},$$

$$\text{where} \quad \overline{\mu}_\mathrm{r} = \frac{\omega^2}{\gamma\mu_\mathrm{m}} \left(\mu_\mathrm{k}(\mu_\mathrm{m} + \mu_\mathrm{k}) + \eta_\mathrm{k}^2\omega^2 \right), \quad \overline{\mu}_\mathrm{i} = \frac{\omega}{\gamma\eta_\mathrm{m}} \left(\mu_\mathrm{k}^2 + \eta_\mathrm{k}(\eta_\mathrm{m} + \eta_\mathrm{k})\omega^2 \right)$$

$$\text{and} \quad \gamma = \left(\frac{\mu_\mathrm{k}}{\eta_\mathrm{m}} - \frac{\eta_\mathrm{k}}{\mu_\mathrm{m}}\omega^2 \right)^2 + \left(\frac{\mu_\mathrm{k}}{\mu_\mathrm{m}} + \frac{\eta_\mathrm{k}}{\eta_\mathrm{m}} + 1 \right)^2 \omega^2.$$

Figure 8 shows a graph of $\overline{\mu}$ against ω and shows that for small ω, the imaginary part is larger than the real part, whilst for larger ω, the real part dominates. In fact, in the limit $\omega \ll 1$,

$$\overline{\mu} = \mathrm{i}\eta_\mathrm{m}\omega + \eta_\mathrm{m}^2 \left(\frac{1}{\mu_\mathrm{m}} + \frac{1}{\mu_\mathrm{k}} \right) \omega^2 + O(\omega^3),$$

i.e. to leading order, the material behaves as if it were governed by a single dashpot with constant η_m. On the other hand, if $\omega \gg 1$,

$$\overline{\mu} = \mu_\mathrm{m} + \mathrm{i}\mu_\mathrm{m}^2 \left(\frac{1}{\eta_\mathrm{m}} + \frac{1}{\eta_\mathrm{k}} \right) \frac{1}{\omega} + O\left(\frac{1}{\omega^2} \right),$$

i.e. to leading order, the material behaves as a perfectly elastic material with spring constant μ_m.

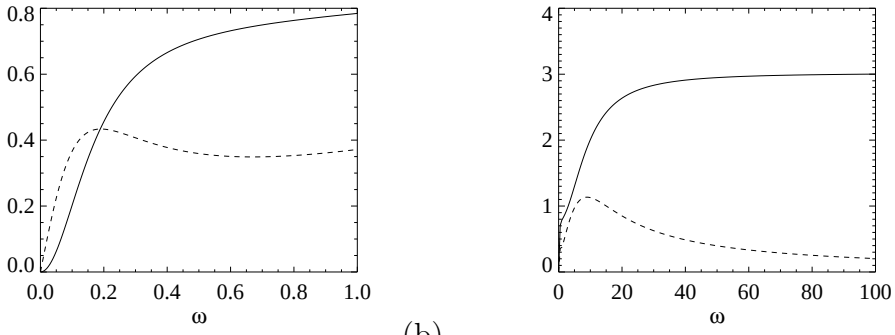

(a) (b)

Figure 8: Graph of the real (solid) and imaginary (dashed) parts of the complex shear modulus against ω, using dashpot and spring constants from [7]. (a) detail near $\omega = 0$; (b) large-ω behaviour.

For small displacements, we may use the equation of linear momentum, which is

$$\rho a\omega^2 \ddot{\mathbf{u}} = \frac{1}{a}\boldsymbol{\nabla}\cdot\boldsymbol{\sigma} \quad \Rightarrow \quad \ddot{\mathbf{u}} = \frac{1}{2}\frac{\overline{\lambda}}{\rho a^2\omega^2}\boldsymbol{\nabla}\boldsymbol{\nabla}\cdot\mathbf{u} + \frac{\overline{\mu}}{\rho a^2\omega^2}\left(\nabla^2\mathbf{u} + \boldsymbol{\nabla}\boldsymbol{\nabla}\cdot\mathbf{u}\right), \quad (36)$$

where $\mathbf{u} = (u_1, u_2, u_3)$ is the material displacement vector from the unstrained state (not to be confused with the velocity field mentioned previously). We have nondimensionalised $\mathbf{u}$ with respect to a, and $\overline{\lambda}$ is the other complex modulus of the material (equivalent to the other Lamé constant). Assuming axisymmetry, the ϕ-component of (36) is

$$-\mathrm{i}\overline{\alpha}^2\ddot{u}_3 = \left(\nabla^2 u_3 - \frac{u_3}{r^2\sin^2\theta}\right),$$

where $\overline{\alpha} = \sqrt{(\mathrm{i}\rho a^2\omega^2/\overline{\mu})}$ is the complex Womersley number. The boundary condition is $u_3 = -\epsilon\sin\theta e^{\mathrm{i}t}$ at $r = 1$, and by analogy with equation (9), the solution is $u_3 = -\epsilon f(r)\sin\theta e^{\mathrm{i}t}$, where $f(r)$ is given by (10). The corresponding WSS is

$$\tau^*_\phi = \frac{1}{2}\mathrm{Re}\left(\overline{\mu}\, r\frac{\partial}{\partial r}\left(\frac{w}{r}\right)\bigg|_{r=1}\right) = \frac{1}{2}\mathrm{Re}\left(-\epsilon\overline{\mu}\,\frac{\partial}{\partial r}\left(\frac{f(r)}{r}\right)\bigg|_{r=1}\sin\theta e^{\mathrm{i}t}\right), \quad (37)$$

to leading order. In the limit $|\overline{\alpha}| \ll 1$

$$\tau^*_\phi = \frac{1}{10}\mathrm{Re}\left(-\mathrm{i}\epsilon\overline{\mu}\,\overline{\alpha}^2\sin\theta e^{\mathrm{i}t}\right)\left(1 + O(\overline{\alpha}^2)\right) = \frac{1}{10}\epsilon\rho a^2\omega^2\sin\theta\cos t\left(1 + O(\overline{\alpha}^2)\right),$$

which is independent of the spring and dashpot constants to leading order. If $\mathrm{Re}(\sqrt{\mathrm{i}\overline{\alpha}}) = \mathrm{Im}(\sqrt{\rho a^2\omega^2/\overline{\mu}}) \gg 1$, we get

$$\tau_\phi^* = \frac{1}{2}\mathrm{Re}\left(-\epsilon\overline{\mu}\frac{\mathrm{i}\overline{\alpha}^2 - 3\sqrt{\mathrm{i}\overline{\alpha}} + 3}{\sqrt{\mathrm{i}\overline{\alpha}} - 1}\sin\theta e^{\mathrm{i}t}\right)\left(1 + O(e^{-\sqrt{2\overline{\alpha}}})\right), \tag{38}$$

$$\sim \frac{1}{2}\epsilon\sqrt{\rho\mu_\mathrm{m}}a\omega\sin\theta\sin t\left(1 + O\left(\frac{1}{\overline{\alpha}}, \frac{\mu_\mathrm{m}}{\eta_\mathrm{m}\omega}, \frac{\mu_\mathrm{m}}{\eta_\mathrm{k}\omega}\right)\right). \tag{39}$$

We will discuss the significance of this result in § 5 below.

4 A model for shear-stress-induced retinal re-detachment

4.1 Introduction and set up of problem

We consider the scenario as depicted in figure 9, in which a weakly spot-welded region in the retina is wedged between two strongly welded regions. Our goal is to determine the displacement field in the weakly welded region in response to a prescribed shear stress applied by the overlying fluid.

We model this region as a homogeneous, isotropic and compressible planar elastic layer. This elastic layer has Young's modulus G, Poisson ratio ν ($-1 < \nu < 1/2$), and its undisturbed thickness and length are H and L, respectively.

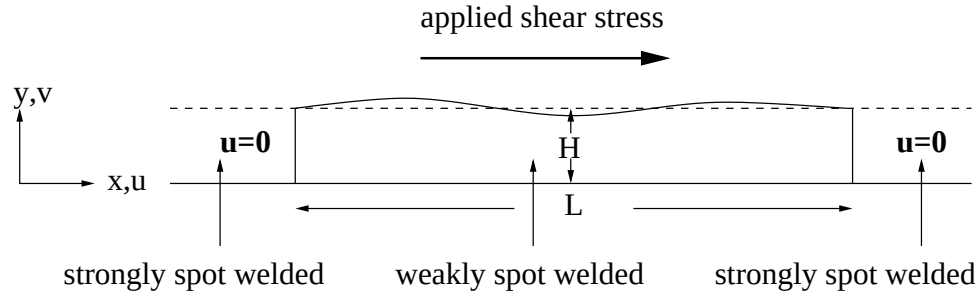

Figure 9: Schematic showing a weakly welded region between two strongly welded regions.

The quasi-steady equilibrium equations are

$$\boldsymbol{\nabla}\cdot\boldsymbol{\sigma} = \mathbf{0}, \quad \boldsymbol{\sigma} = \frac{\nu G}{(1+\nu)(1-2\nu)}\mathrm{tr}(\mathbf{E})\mathbf{I} + \frac{G}{(1+\nu)}\mathbf{E}, \tag{40}$$

where $\boldsymbol{\sigma}$ and $\mathbf{E}$ are the stress and strain tensors, respectively. $\mathbf{E}$ is related to the displacement field by

$$\mathbf{E} = \begin{bmatrix} u_x & \frac{1}{2}(u_y + v_x) \\ \frac{1}{2}(u_y + v_x) & v_y \end{bmatrix}, \tag{41}$$

where $\mathbf{u} = (u, v)$ is the displacement field. Substituting (41) into (40a) gives the displacement field formulation of the equilibrium equations

$$\frac{G}{(3-\delta)}\left[(1+\delta)\boldsymbol{\nabla}\boldsymbol{\nabla}\cdot\mathbf{u} - \delta\boldsymbol{\nabla}\times\boldsymbol{\nabla}\times\mathbf{u}\right] = 0, \tag{42}$$

where $\delta = 1 - 2\nu$. In component form, the above equation can be re-written as

$$\frac{G}{(3-\delta)}[(1+\delta)(v_{yy} + v_{xx}) + u_{yx} - v_{xx}] = 0, \tag{43a}$$

$$\frac{G}{(3-\delta)}[\delta(u_{yy} + u_{xx}) + v_{yx} + u_{xx}] = 0, \tag{43b}$$

subject to the boundary conditions

$$\left.\begin{array}{r} \frac{G}{(3-\delta)}\left[\left(\frac{1}{\delta} - 1\right)(v_y + u_x) + 2v_y\right] = 0 \\ \frac{G}{(3-\delta)}(v_x + u_y) = S(x) \end{array}\right\} \quad \text{on } y = H, \tag{44a}$$

$$u = \frac{\alpha G}{(3-\delta)}(v_x + u_y) \quad \text{and} \quad v = 0 \quad \text{on } y = 0, \tag{44b}$$

$$u = v = 0 \quad \text{for } x < 0 \text{ and } x > L. \tag{44c}$$

Here S is a prescribed shear stress and α is a "slip" parameter. (44a) imposes continuity of normal and shear stresses at the layer free surface $y = H$, while (44b) allows the layer to slip at $y = 0$.

4.2 "Outer" problem

A long-wavelength approximation can be utilised to simplify the above equations assuming that the layer thickness is much smaller than its length, *i.e.* $H \ll L$. This is only an outer solution to the above problem since at the boundaries variations in both x and y directions may be comparable, where this approximation is not valid.

The problem is nondimensionalised as follows:

$$x = Lx^\star, \quad y = Hy^\star, \quad (u, v) = \frac{(3-\delta)}{\mathcal{G}}H(u^\star, v^\star), \quad S = S_1 S^\star \tag{45}$$

where $\mathcal{G} = G/S_1$ and S_1 is some characteristic shear stress scale. We can then re-write the governing equations as (dropping the stars)

$$(1+\delta)(v_{yy} + \phi^2 v_{xx}) + \phi u_{yx} - \phi^2 v_{xx} = 0, \tag{46a}$$

$$\delta(u_{yy} + \phi^2 u_{xx}) + \phi v_{yx} + \phi^2 u_{xx} = 0, \tag{46b}$$

subject to the boundary conditions

$$\left(\frac{1}{\delta} - 1\right)(v_y + \phi u_x) + 2v_y = 0, \quad \phi v_x + u_y = S, \quad \text{on } y = 1, \tag{47a}$$

$$u = \beta(u_y + \phi v_x), \quad v = 0, \quad \text{on } y = 0, \tag{47b}$$

where $\phi = H/L \ll 1$ and $\beta = \alpha G/[(3-\delta)H]$.

We perform a leading-order analysis neglecting terms that are order ϕ or smaller enabling us to reduce the above equations to a much simpler form. We consider the cases corresponding to $\delta \sim 1$ (compressible layer), $\phi^2 \ll \delta \ll 1$ (almost incompressible layer) and $\delta \sim \phi^2$ (incompressible layer). A composite formula is then determined which is uniformly valid for all δ.

Case 1: Compressible layer ($\delta \sim 1$)

The leading order equations are

$$v_{yy} = u_{yy} = 0,$$

together with the boundary conditions

$$v_y = 0, \quad u_y = S, \quad \text{on } y = 1,$$
$$u = \beta u_y, \quad v = 0, \quad \text{on } y = 0,$$

which have the solution

$$u = S(y + \beta), \quad v = 0.$$

Case 2: Almost incompressible layer ($\phi^2 \ll \delta \ll 1$)

For this case, the leading order equations are

$$v_{yy} = (u_y + v_x)_y = 0,$$

with boundary conditions

$$v_y = 0, \quad u_y = S, \quad \text{on } y = 1,$$
$$u = \beta u_y, \quad v = 0, \quad \text{on } y = 0.$$

These have solution

$$u = S(y + \beta), v = 0.$$

Case 3: Incompressible layer ($\delta \sim \phi^2$)

The scalings are motivated by the incompressibility criterion which suggests that $v_y \sim \phi u_x$. This forces v to be order ϕ. Letting $u_x + v_y = -p$, we obtain at leading order

$$p_y = u_{yy} - p_x = 0,$$

with boundary conditions

$$\begin{aligned} p = 0, \quad u_y = S, \quad \text{on } y = 1, \\ u = \beta u_y, \quad v = 0, \quad \text{on } y = 0. \end{aligned}$$

These have solution

$$p = 0, u = S(y + \beta), v = -\phi S_x \left(\frac{y^2}{2} + \beta y \right).$$

A composite formula can then be written, valid uniformly for all δ, as follows:

$$u = S(y + \beta), \quad v = -\phi S_x \left(\frac{y^2}{2} + \beta y \right) \approx 0. \tag{48}$$

Hence, to leading order in this region, the only displacement is due to the stretching of the layer by the prescribed shear stress. In addition, compressibility does not influence the deformation of the layer owing to the absence of a normal stress on the layer free surface.

4.3 "Inner" problem

Since we expect variations along the x and y directions to be comparable at the boundaries, the long-wavelength approximation is not valid here. Hence, the full 2D problem ((43) and (44)) needs to be solved here. This is beyond the scope of this report.

5 Discussion

In this report, we have investigated the form of the flows in a post-vitrectomy eye, generated by buoyancy forces and saccadic motions. In the buoyancy-driven case, which was considered in §2, we found the leading order balance in the governing equations in the case $R \ll 1$. This gave rise to a zenithal WSS of size $\mu\kappa R/a^2$.

We also studied the fluid flow induced by torsional oscillations in a sphere in §3. We estimated the WSS and also studied the fluid dynamics in two special cases, which were I: $\epsilon \ll 1$ and $\alpha = O(1)$, and II: $\alpha \gg \epsilon^{-1} \gg 1$. We found the solutions as series expansions in a small parameter in each case. In §3.3, we considered case I, finding that if α is small, the fluid moves almost as a solid body, giving rise to an azimuthal WSS of order $\epsilon\mu\omega$, whilst for larger α, (moving towards case II), the fluid motion becomes confined to a boundary layer at the wall of the sphere; the fluid in the interior remains almost stationary. This gives rise to a larger WSS of order $\epsilon\alpha\mu\omega$.

In §3.4, we considered case II, finding that, as predicted in §3.3, a boundary layer forms at the wall of the sphere, which itself has a two-layer structure. The inner layer is of width α^{-1}, and in it, the amplitude of the azimuthal fluid flow decays exponentially fast away from the wall. However, the centrifugal forces generated by the azimuthal flow have a steady component that does not decay away from the wall. In turn, these give rise to a smaller steady streaming flow, in which the fluid moves in the zenithal direction from the poles to the equator. To satisfy continuity, it is accompanied by a radial flow from the equator into the interior, and also a radial flow from the interior toward the poles. The WSS induced by the flows are of size $\epsilon\alpha\mu\omega$ and $\epsilon^2\alpha\mu\omega$ in the azimuthal and zenithal directions respectively. These steady streaming flows drive fluid motion with velocities $O(\epsilon^2)$ throughout the interior of the sphere. We predict that the stream surfaces will consist of two sets of nested tori, in the northern and southern hemispheres respectively, as shown in figure 6.

In §3.5, we did a similar calculation for the fluid dynamics of human vitreous humour in the limit $\epsilon \ll 1$, corresponding to case I, but accounting for viscoelastic effects. This gave an azimuthal WSS of size $\epsilon\rho a\omega^2$ for small ω, and $\epsilon\sqrt{\rho\mu_{\mathrm{m}}}a\omega$ when ω is sufficiently large.

For the activities discussed in the introduction, we can now estimate the azimuthal WSS for post-vitrectomy eyes, using equation (11), and the zenithal WSS using equation (23). For normal eyes, we may estimate the azimuthal WSS using (37). The maximum values of the functions obtained, along with the corresponding values of α, $\overline{\mu}$, $|\overline{\alpha}|$ and $\mathrm{Re}(\sqrt{\mathrm{i}}\overline{\alpha})$ are given in table 1. On comparing the post-vitrectomy values of τ_ϕ^* given in table 1 with the values that would be obtained if instead we used the $\alpha \ll 1$ and $\alpha \gg 1$ approximations, given in formulae (12) and (13) (or equivalently (22)) respectively, we see that the $\alpha \gg 1$ approximation provides a very accurate estimate. Similarly for normal eyes, if we compare the values of τ_ϕ^* in table 1 with those obtained using the $|\alpha| \ll 1$ and $\mathrm{Re}(\sqrt{\mathrm{i}\alpha}) \gg 1$ approximations as in (37) and (39), we see that, with the exception of the case of turning

			Values in post-vit. eye			Values in normal eye			
Activity	ϵ	ω	α	$\max(\tau_\phi^*)$	$\max(\tau_\theta^*)$	$\overline{\mu}$	$\lvert\alpha\rvert$	$\mathrm{Re}(\sqrt{\mathrm{i}}\overline{\alpha})$	$\max(\tau_\phi^*)$
Turning eyes to look at object [13]	$\pi/9 \approx 0.35$	$(20\pi/9)\cdot(9/\pi) = 5$	30	0.017	0.0015	$1.3 + 1.0\mathrm{i}$	1.4	0.43	0.11
Reading [14]	$7.685\pi/150 \approx 0.16$	$20\pi \approx 63$	110	0.37	0.015	$3.0 + 0.3\mathrm{i}$	13	0.68	2.0
MSWI[1]	$0.7\pi/180 \approx 0.012$	$27000/0.7\pi \approx 12000$	1500	75	0.23	$3.0 + 0.0\mathrm{i}$	2500	0.68	48
REM [10]	$\pi/36 \approx 0.087$	$50\cdot 36/\pi \approx 570$	320	5.4	0.12	$3.0 + 0.0\mathrm{i}$	110	0.68	25
SEM [10]	$\pi/36 \approx 0.087$	$20\cdot 36/\pi \approx 230$	200	1.36	0.30	$3.0 + 0.1\mathrm{i}$	46	0.68	8.8

Table 1: Estimated values of amplitude, frequency, Womersley number and WSS for various activities in both post-vitrectomy and normal eyes. S.I. units are used, so ω is measured in s^{-1}; $\overline{\mu}$, τ_ϕ^* and τ_θ^* are measured in $\mathrm{kg\,m^{-1}\,s^{-2}}$; and α is dimensionless. We have used $\rho = 1000\,\mathrm{kg\,m^{-3}}$ for both water and vitreous humour.

one's eyes to look at an object, the limit $\mathrm{Re}(\sqrt{\mathrm{i}\alpha}) \gg 1$ provides a reasonably accurate approximation. Thus the case considered in §3.4 is realistic for the activities considered. As expected, the azimuthal component of the WSS is much greater than the zenithal component. Comparing these values with the estimated WSS for buoyancy-driven motion, we see that the WSS induced by monophasic square wave intrusions (MSWI) is much greater even than the worst case estimates for the WSS induced by buoyancy driven flow, which was $0.7\,\mathrm{kg\,m^{-1}\,s^{-2}}$ for the case $R \ll 1$, and for more probable values of Δ_T, the WSS in rapid and slow eye movement (REM and SEM) will also be bigger. **Hence, we tentatively conclude that the saccade-driven motion of the fluid is likely to induce a much greater WSS than the buoyancy driven motion, and hence likely to be the more important factor in RD.**

In most cases, the WSS is greater in normal eyes than in post-vitrectomy eyes, the only exception being MSWI! This is due to the very large effective viscosity of human vitreous humour, which pre-multiplies the WSS. Thus these results would tentatively suggest that perhaps fluid motion due to saccadic eye movement is not the instigating effect causing the re-detachment of the retina, though it may be the effect that causes an already weakened post-operative retina to detach from the choroid. However, if this is the case, there would have to be other non-fluid-dynamical forces that weaken the post-vitrectomy retina.

In a similar way, if we were able to do the calculation for buoyancy-driven flow with human vitreous, we would presumably see a similar effect, since the effective viscosity would still pre-multiply the WSS. Thus further explanations for the problem of retinal re-detachment need to be found.

Finally, we studied a model of the deformation of the retina under an applied WSS. We showed that the major part of the weakly welded section will undergo stretching with possible buckling near the boundaries. This buckling solution can only be obtained by solving the full 2D equations near the boundaries. This shear-stress-induced buckling may lead to possible re-detachment of the retinal layer.

References

[1] R. V. Abadi & E. Gowen. Characteristics of saccadic intrusions, *Vision Res.*, **44**, 2675–2960 (2004).

[2] A. T. Bahill, M. R. Clark & L. Stark. The main sequence, a tool for studying human eye movements, *Math. Biosci.*, **24**, 191–204 (1975).

[3] C. R. Canning, M. J. Greaney, J. N. Dewynne & A. D. Fitt. Fluid flow in the anterior chamber of a human eye, *IMA J. Math. Appl. Med.*, **19(1)**, 31–60 (2002).

[4] T. David, S. Smye, T. Dabbs & T. James. A model for the fluid motion of vitreous humour of the human eye during saccadic eye movement, *Phys. Med. Biol.*, **43**, 1385–1399 (1998).

[5] A. Gopinath. Steady streaming due to small amplitude torsional oscillations of a sphere in a viscous fluid, *Q. J. Mech. Appl. Math.*, **46**, 501–521 (1993).

[6] R. Hollerbach, R. J. Wiener, I. S. Sullivan, R. J. Donnelly and C. F. Barenghi. The flow around a torsionally oscillating sphere, *Phys. Fluids*, **14(12)**, 4192–4205 (2002).

[7] B. Lee, M. Litt & G. Buchsbaum. Rheology of the vitreous body. Part I: Viscoelasticity of human vitreous, *Biorheology*, **29**, 521–533 (1992).

[8] S. P. Liversedge & J. M. Findlay. Saccadic eye movements and cognition, *Trends Cogn. Sci.*, **4(1)**, 6–14 (2000).

[9] W. H. Lyne. Unsteady viscous flow in a curved pipe, *J. Fluid Mech.*, **45**, 13–31 (1971).

[10] H. S. Porte. Slow horizontal eye movement at human sleep onset, *J. Sleep Res.*, **13**, 239–249 (2004).

[11] N. Riley. Oscillatory Viscous Flows. Review and Extension, *J. Inst. Maths Applics.*, **3**, 419–434 (1967).

[12] N. Riley. Steady Streaming, *Annu. Rev. Fluid Mech.*, **33**, 43–65 (2001).

[13] K. G. Rottach, V. E. Das, W. Wohlgemuth, A. Z. Zivotofsky & R. J. Leigh. Properties of horizontal saccades accompanied by blinks, *J. Neurophysiol.*, **79(6)**, 2895–2902 (1998).

[14] S.-N. Yang & G. W. McConkie. Eye movements during reading: a theory of saccadic initiation times, *Vision Res.* **41**, 3567–3585 (2001).